An edited version of this paper was published in *Computers & Geosciences (doi:* 10.1016/j.cageo.2014.10.002)

Inflow-outflow boundary conditions along arbitrary directions in Cartesian lake models

Ramón, C. L. [(a), (b), (e)], A. Cortés [(a), (c)] and F. J. Rueda [(a), (d)]

[(a)] Water Research Institute and Department of Civil Engineering, University of Granada. C/Ramón y Cajal, 4 - 18071 Granada, Spain. Telephone: (+34) 958 248325 ([b] crcasanas@ugr.es, [c] ccalicia@ugr.es, [d] fjrueda@ugr.es). [(e)] Corresponding author.

Abstract

Specifying point sources and sinks of water near boundaries is presented as a flexible approach to prescribe inflows and outflows along arbitrary directions in Cartesian grid lake models. Implementing the approach involves a straightforward modification of the governing equations, to include a first order source term in the continuity and momentum equations. The approach is implemented in a Cartesian grid model and applied to several test cases. First, the flow along a straight flat bottom channel with its axis forming different angles with the grid directions is simulated and the results are compared against well-known analytical solutions. Point-sources are then used to simulate unconfined inflows into a reservoir (a small river entering a reservoir in a jet-like manner), which occur at an angle with the grid directions. The model results are assessed in terms of a mixing ratio between lake and river water, evaluated at a cross section downstream of the inflow boundary. Those results are particularly sensitive to changes in the inflow angle. It is argued that differences in mixing rates near the inflow sections could affect the fate of river-borne substances in model simulations.

Keywords

Three dimensional (3D) simulation; Cartesian grid; inflow angle; source-sink cell; mixing; lake

3D-SWE = Three-dimensional shallow water equations
SC = Sources and sinks
NF = Normal velocity component along faces
SML = Surface mixed layer

1. Introduction

The space-time distribution of particulate and dissolved substances in lakes and reservoirs, the light and nutrient availability for algal growth and, in general, the environment in which biogeochemical reactions occur are largely controlled by transport and mixing processes in the water column. Describing and understanding the physical processes leading to mixing and transport in the water column, hence, is the first step that needs to be taken to understand the chemical and biological properties of aquatic ecosystems, and its spatial and temporal variability. To this end, considerable efforts have been devoted during the last few years to develop and apply numerical models, capable of solving the governing equations of fluid motion and, hence, describing the flow environment in three-dimensions with a high temporal and spatial resolution and low computational cost. Most of these large-scale flow models are based on the solution of the three-dimensional form of the shallow-water equations 3D-SWE, subject to the appropriate boundary conditions. The correct representation of the specific flow patterns that develop in any given water body depends mainly on the ability of the model to represent accurately the mass and energy fluxes (their frequency, intensity, duration and timing) that occur through the free surface − and which are the drivers of motion in the water column − and the morphometry of the system (Imboden and Wüest, 1995). This, in turn, largely depends on how the physical space is discretized on the model grid (grid system). The most widely used grid system in 3D lake modeling is the Cartesian-grid (e.g. Hodges et al., 2000; Rueda et al., 2003; Appt et al., 2004; Laval et al., 2005; Okely and Imberger, 2007; Hoyer et al., 2014a, b). Model coding and grid definition in this grid-system is much simpler than in others. Grid generation, for example, in unstructured-grid models is not a completely automatic process, requiring separate grid creation software, and user intervention is often need to produce a grid of satisfactory quality (Liang et al., 2007), especially if complex topographic features are present. It is also computationally expensive.

In spite of their simplicity, Cartesian grid lake models tend to produce locally inaccurate solutions where the shoreline is not aligned with the Cartesian grid directions and is represented as a staircase. A variety of approaches have been proposed to resolve correctly the near shore circulation. The grid resolution can be increased near the shoreline, for example, using ‘plaid’ structured meshes (i.e. non-uniform Cartesian grid spacing), adaptive mesh refinements or nested grids (e.g. Berger and Oliger, 1984; Ham et al., 2002; Gibou et al., 2007; Peng et al., 2010, and references therein). Cut cells can also be used for the solution of the shallow water equations (Causon et al., 2000; Liang et al., 2007), and in this case, boundary contours are cut out of a background Cartesian mesh and cells that are partially or completely cut are singled out for special treatment. Other approaches such as the immerse boundary method of Peskin (1972, 2002), the virtual boundary method (Saiki and Biringen, 1996) or the Brinkman penalization method (e.g. Reckinger et al., 2012) introduce a source (force) term in the momentum equations, to represent the force exerted by solid boundaries on the fluid.

An additional problem arising from the Cartesian representation of lake boundaries is related to the simulation of river inflows and outflows, which may not be aligned with the grid directions (Fig. 1). Flow boundary conditions (clamped boundary conditions) are typically prescribed in lake models (e.g. Smith, 2006; Hodges et al., 2000) by setting the values of the velocity components normal to the grid directions at the faces of the boundary cells (Fig 1). Flow directionality with this approach, which will be referred to as NF-method (for normal velocity component along faces), could be wrong. The effects of inflows on circulation and mixing − whether these effects are localized (Rueda and Vidal, 2009) or if they impact the basin-scale motions (Hollan, 1998) − or the fate of river-borne substances, may not be correctly simulated with the NF-method. Our goal is to present an alternative approach to specifying inflow and outflow boundary conditions in Cartesian lake models, in which flow direction is independent of grid alignment. It consists of using point sources and sinks of mass and momentum in grid cells which are next to solid boundaries, where water is added or detracted from the computational domain (Fig. 1). This approach, here referred to as SC (for sources and sinks), implies a simple-to-implement modification of the governing equations. The grid, in turn, does not need to be modified. The use of sources- and sinks- of mass and momentum has been successfully applied in the lake modeling literature (Singleton et al. 2010) to simulate the effect of bubble-plumes on lake circulation, and, hence, on hypolimnetic oxygen and density fields. Here, the method is adapted to represent the effect of localized flows into and out of the domain, with length scales which are well below the grid resolution of the model. It is examined whether ignoring the directionality of inflows may affect or not the results of local and larger basin-scale simulations of mixing and transport in lakes and reservoirs.

2. Methods

2.1. Approach

The SC and the NF approaches to specifying flow boundaries in a 3D-SWE model will be first described. These two approaches were compared in a test case in which the flow boundaries are aligned with the grid directions. The test consists on the simulations of the flow field along a straight rectangular channel with flat bottom laid out along the x-axis. The SC-method will be then applied to the same straight channel, but in this case, the channel will be assumed to form an angle with the Cartesian grid directions. The SC-method will be then applied to simulate environmental flows in a lake in which the use of boundaries not aligned to the Cartesian grids are needed.

2.2. Governing equations with point sources and sinks of fluid.

Assuming that (1) variations in density are negligible everywhere except in the buoyancy term (the Boussinesq approximation), (2) the weight of the fluid balances the pressure in the equation for vertical momentum (the hydrostatic approximation), and (3) a diffusion-like term can be used to represent turbulent fluxes of scalars and momentum (the eddy diffusivity concept), the Navier-Stokes equations, incorporating point sources and sinks of fluids, can be written as (adapted from the work of Lynch,1986):

$$\frac{\partial u}{\partial x}+\frac{\partial v}{\partial y}+\frac{\partial w}{\partial z}=\frac{\delta}{\rho_0} \tag{1}$$

$$\frac{\partial \zeta}{\partial t}+\frac{\partial}{\partial x}\left[\int_{-D}^{\zeta} u dz\right]+\frac{\partial}{\partial y}\left[\int_{-D}^{\zeta} v dz\right]=\int_{-D}^{\zeta}\frac{\delta}{\rho_0}dz \tag{2}$$

$$\begin{aligned}\frac{\partial u}{\partial t}+u\frac{\partial u}{\partial x}+v\frac{\partial u}{\partial y}+w\frac{\partial u}{\partial z}-fv=-\left(g\frac{\partial \zeta}{\partial x}+g\frac{1}{\rho_0}\int_{z}^{\zeta}\frac{\partial \rho}{\partial x}dz'\right)+\\ \frac{\partial}{\partial x}\left(A_h\frac{\partial u}{\partial x}\right)+\frac{\partial}{\partial y}\left(A_h\frac{\partial u}{\partial y}\right)+\frac{\partial}{\partial z}\left(A_v\frac{\partial u}{\partial z}\right)+\frac{\delta}{\rho_0}(u-u_0)\end{aligned} \tag{3}$$

$$\begin{aligned}\frac{\partial v}{\partial t}+u\frac{\partial v}{\partial x}+v\frac{\partial v}{\partial y}+w\frac{\partial v}{\partial z}+fu=-\left(g\frac{\partial \zeta}{\partial y}+g\frac{1}{\rho_0}\int_{z}^{\zeta}\frac{\partial \rho}{\partial y}dz'\right)+\\ \frac{\partial}{\partial x}\left(A_h\frac{\partial v}{\partial x}\right)+\frac{\partial}{\partial y}\left(A_h\frac{\partial v}{\partial y}\right)+\frac{\partial}{\partial z}\left(A_v\frac{\partial v}{\partial z}\right)+\frac{\delta}{\rho_0}(v-v_0)\end{aligned} \tag{4}$$

$$\frac{\partial \theta}{\partial t}+u\frac{\partial \theta}{\partial x}+v\frac{\partial \theta}{\partial y}+w\frac{\partial \theta}{\partial z}=K_h\frac{\partial^2 \theta}{\partial x^2}+K_h\frac{\partial^2 \theta}{\partial y^2}+\frac{\partial}{\partial z}\left(K_v\frac{\partial \theta}{\partial z}\right)+\frac{H}{\rho c_p}+\frac{\delta}{\rho_0}\theta_0 \qquad (5)$$

$$\frac{\partial O}{\partial t}+u\frac{\partial O}{\partial x}+v\frac{\partial O}{\partial y}+w\frac{\partial O}{\partial z}=K_h\frac{\partial^2 O}{\partial x^2}+K_h\frac{\partial^2 O}{\partial y^2}+\frac{\partial}{\partial z}\left(K_v\frac{\partial O}{\partial z}\right)+\frac{\delta}{\rho_0}O_0 \qquad (6)$$

These equations comprise the 3D-SWE. They express the physical principles of conservation of mass for an incompressible fluid (Eqs. 1-2), conservation of momentum (Eqs. 3-4) and conservation of energy (Eq. 5). Finally, Eq. 6 is the transport equation for passive tracers, not affecting the fluid density. Here u, v, and w represent the velocity components in the x-, y-, and z- directions; f is the Coriolis parameter; g is the acceleration of gravity; θ represents temperature; O represents the concentration of a passive tracer in the domain; ζ is the free surface elevation; $z = -D(x, y)$ is the depth of the bottom boundary measured from the undisturbed free surface $z = 0$; H is a source of heat associated with heat and energy fluxes due to atmospheric heating or cooling; A is the kinematic eddy viscosity and K is the turbulent transfer coefficient (eddy diffusivity) for temperature. The density ρ is calculated from temperature using an equation of state; the subscript h and v refer to horizontal and vertical directions, respectively; δ denotes the fluid source strength, and the ratio δ/ρ_0, for a given computational source cell of nominal volume ($= \Delta x \times \Delta y \times \Delta z$), represents the volume of water added/detracted per unit time, divided by the nominal volume of the cell. Note that this term will only be non zero next to the boundaries where inflows and outflows are specified. The subscript 0 in Eqs. 1-6 is intended to define the characteristics of the water being added or removed from the computational domain at a source or sink cell. The SC-method consists of setting source-sink computational cells adjacent to the flow boundaries in which water is added or detracted from the domain. Note first that, as a result of the source-sink term in the continuity equations − representing the addition and detraction of water from the domain−, the free surface elevation rises and descends and, hence, pressure gradients are generated near the boundaries. The velocity direction of the inflowing or out-flowing water (for example, inflows entering at an angle into a lake) can be prescribed by conveniently specifying u_0 and v_0. The larger is the source strength, the closer the velocity solution will be to u_0 and v_0.

2.3. Hydrodynamic model

The SC-method was implemented and tested in a 3D-SWE model (Smith, 2006), which has been previously used and validated against analytical solutions and field data sets collected in a variety of environments (Rueda and Cowen, 2005; Rueda and MacIntyre, 2010 and references therein). The governing equations (1-6) are first posed in layer-averaged form by integrating over the height of a series of horizontal layers separated by level planes. The layer-averaged momentum equations are solved using a semi-implicit, three-level, iterative leapfrog-trapezoidal finite difference scheme on a staggered Cartesian grid. The semi-implicit approach is based on treating the gravity wave and vertical diffusion terms in the momentum equations implicitly to avoid time-step limitations due to gravity-wave CFL conditions, and to guarantee stability of the method. All other terms, including advection, are treated explicitly. The leapfrog-trapezoidal algorithm used for time stepping gives second order accuracy both in time and space. The variables are arranged in space on a C-Arakawa staggered Cartesian grid, with the flow variables defined at the interfaces, and the scalars and the pressure at the cell centers (Fig. 1). Non-active (i.e. tracers) and active (i.e. temperature) scalar transport equations were solved using a two-level semi-implicit scheme, in which only vertical diffusion is discretized implicitly. The advection terms in the transport equation for scalars are discretized with flux-limiter methods (e.g. Durran, 1999). Turbulent mixing is represented in the 3-D model using diffusion-like terms. A Laplacian operator with constant mixing coefficients (horizontal eddy viscosity A_h or diffusivity K_h) is used in the model to represent horizontal mixing of momentum and scalars. Vertical eddy coefficients of mixing K_v are calculated using a two-equation model originally proposed by Mellor and Yamada (1974), and later modified by Kantha and Clayson (1994). This turbulent modeling approach is typically used in large scale models for geophysical flows due to their reduced computational burden. The discretized form of the depth-averaged continuity equation, governing the changes in the free-surface elevation (Eq. 2) is given by

$$\begin{aligned}\zeta_{i,j}^{n+1} = \zeta_{i,j}^{n-1} &- \frac{\Delta t}{\Delta x}\left[\sum_{k=k_1}^{km}\left(U_{i+1/2,j,k}^{n+1} - U_{i-1/2,j,k}^{n+1} + U_{i+1/2,j,k}^{n-1} - U_{i-1/2,j,k}^{n-1}\right)\right] \\ &- \frac{\Delta t}{\Delta y}\left[\sum_{k=k_1}^{km}\left(V_{i,j+1/2,k}^{n+1} - V_{i,j-1/2,k}^{n+1} + V_{i,j+1/2,k}^{n-1} - V_{i,j-1/2,k}^{n-1}\right)\right]\end{aligned} \qquad (7)$$

Here, U and V are the volumetric transport in x- and y- directions, respectively; Δt is the time step, Δx and Δy are the horizontal size of a cell in x- and y-, respectively; subscripts (i, j, k) denote the spatial location in the computational grid, and the superscripts (n), the time t level at which the variable is evaluated. The symbols k_1 and k_m denote the first (shallowest) and last (deepest) layer in a water column respectively. In the course of the computations for a given time step, the volumetric transports at time n+1 in the momentum equations are expressed as a function of the free surface at that time, i.e. $U^{n+1} = f(\zeta^{n+1})$ and $V^{n+1} = g(\zeta^{n+1})$ (see Table 1), and substituted in Eq. 7 to yield a sparse symmetric positive-definite system of equations for ζ^{n+1}. The matrix problem is then solved using a conjugate gradient iterative method (see Smith, 2006, for details). Flow boundaries in the NF-approach are prescribed by setting the values of volumetric transports in Eq. 7 to their known values. These, in turn, are estimated from observed flow rates Q_{FB}, assuming a uniform distribution of velocities along the flow boundaries. In the SC-approach, instead, a source-sink term (Table 1) is added to $f(\zeta^{n+1})$ or $g(\zeta^{n+1})$ in the momentum equations during the solution process. Distinguishing between boundaries acting as sources (inflows) or sinks (outflows) is done by prescribing positive or negative flows Q_{FB} at the boundary cells, respectively. Flows are prescribed on the E face of a computational cell by adding the source term (E) given in Table 1, to $f(\zeta^{n+1})$ in the momentum equations for the volumetric transport U at (i+1/2, j). Flows across the N face (i, j+1/2) are prescribed by adding the source term (N) to $g(\zeta^{n+1})$ in the momentum equations for the volumetric transport V at (i+1/2, j). Note that those source-sink terms can only be added to faces within the computational domain, for which momentum equations are being solved. Note also, that the source terms include fractions of the total flow entering in a given water column, that flow across the E and N faces (α_E and α_N in Table 1, respectively).

2.4 Simulations in a straight channel aligned with the Cartesian grid

The steady-state flow through an 8-m long straight channel of rectangular cross section and flat bottom was simulated in this first test (Fig. 2). The channel was 1m wide, and the water column was initially 0.6 m deep. The computational cells were (Δx, Δy, Δz) = (0.1, 0.1, 0.12) m in the x-, y- and z- directions, respectively, with a total number of wet grid cells of 10, 80 and 5 in each direction. The time step Δt was set to 0.2 s to meet the advection Courant number criterion ($C_a \leq 1$). For these runs C_a (= $u\Delta t/\Delta x$) was O (10^{-1}). Flow boundary conditions were set both at the inflow and outflow sections. Flow rates in and out of the domain were both equal and fixed to 0.18 $m^3 s^{-1}$ in all cases. The water was initially quiescent and the model was run until steady state. In this first series of simulations (A-simulations) the channel was aligned with the *x*-grid direction (Fig. 2) and, thus, the flow boundaries were specified normal to the E- and W-boundaries. Both the NF- and the SC- approaches were used to represent flow boundaries.

The slope of the free surface I along the channel in this problem should follow the expression (see Chaudhry, 1993, for example):

$$I = \frac{\zeta_1 - \zeta_2}{L} = \frac{S_0 - S_f}{1 - Fr^2} \tag{8}$$

Here ζ_1 and ζ_2 represent the water free surface elevation at the entrance and at the end of the channel, respectively, L is the channel length, S_0 is the bottom slope, and S_f is the longitudinal slope due to friction. The Froude number Fr is defined in terms of the mean streamwise velocity u_s, the acceleration of gravity g, and the depth D of the channel, $Fr = u_s/(gD)^{1/2}$. The frictional slope, in turn, was estimated as $S_f = C_d\, Fr^2$. If the bottom is level, $S_0 = 0$. Under subcritical conditions ($Fr < 1$), such in this case, the water surface elevation decreases in the flow direction ($I < 0$). The free surface solutions of the model were compared against the theoretical result given by Eq. 8. The error in the free surface solution was quantified using the bias ε, which is defined in terms of the theoretical I_t and the modeled I_i slopes as

$$\varepsilon_I = \frac{(I_i - I_t)}{I_t} \cdot 100 \tag{9}$$

The simulated slopes were estimated from the free surface solution at all computational cells existing 1 m away from the boundaries. Velocity and vertical eddy viscosity profiles calculated with the NF- and SC- approaches were compared at several points located at the center of the domain (Section b in Fig. 2) or close to the boundaries (Sections a and c in Fig. 2). The differences between approaches were quantified as

$$\varepsilon_p = \frac{\sqrt{\dfrac{\sum_{i=2}^{km}\left(\psi_i - \psi_{i,0}\right)^2}{km-1}}}{\overline{\psi_0}} \cdot 100 \qquad (10)$$

Here Ψ represents laterally-averaged values (either velocities or K_v), and the subscript 0 refers to values of the reference simulation, here taken as that conducted with the NF-method. The overbar represents depth-averaged values. Note that the error is given in non-dimensional form, as a percentage of the mean laterally-averaged value of a given variable in a given section.

The simulations were run with different values of C_d ranging from O(10^{-3}) to O(10^{-1}) and constant horizontal eddy diffusivities (K_h) of 10^{-2} ms^{-2} (Table 2). The model was set to run (also valid for sections 2.5-2.6) using a second-order space-centered method for momentum advection and 2 trapezoidal iterations, without smoothing of the leapfrog solution.

2.5 Simulations in a straight channel at an angle with the grid

On a second series of simulations, the channel was rotated 45^{o} anticlockwise relative to the x-axis (Fig. 2). This channel is referred to as the B-channel, and the simulations conducted are referred to as the B-simulations (Table 2). Note that, in this case, the lateral boundaries are not straight lines, but are represented as a staircase, which might affect the solution. The flow boundary conditions were prescribed using the SC-method, with velocities aligned with the main axis of the channel. In these B-simulations, though, the total flow was split in equal parts across the N and E faces of the boundary cells (α_N = 0.5 and α_E = 0.5). The same values for C_d and constant K_h as in the A-simulations were used here. Three more grids were tested with higher ($\Delta x = \Delta y$ = 0.05 m, with 16430 wet grid cells, and $\Delta x = \Delta y$ = 0.01 m, with 399035 wet grid cells) and lower ($\Delta x = \Delta y$ = 0.2 m, with 995 wet grid cells) resolution in the horizontal to assess the effects of the staircase representation of the channel banks − as a result of the use of a Cartesian grid − on the modeled free surface slope. The time step Δt was set to 0.5 s, 0.01s and 0.002 s at simulations with the 0.2 × 0.2 m, the 0.05 × 0.05 m and the 0.01 × 0.01m resolution grids, respectively, to meet the criterion $C_a \leq 1$. To compare these results with those with A-simulations, the simulated results within the first and last meters of the channel length were ignored, to avoid the influence of the boundary conditions. Velocity profiles calculated in the B-simulations were also compared at the center of the domain (Section b in Fig. 2) with those calculated in the A-simulations using the NF-method for boundary conditions. The solutions near the boundaries (Sections a and c in Fig. 2) were also compared.

2.6. Simulations of laterally-unconfined inflows to a lake

The model was used to simulate near-field (initial) mixing and transport processes associated to a negatively buoyant inflow, the Izbor River, into a small reservoir, Lake Béznar (36º55'N, 3º31'W, Fig. 3a), in southern Spain. The reservoir has a maximum depth of 83.7 m at the dam, and a maximum length of ~4 km. The bottom slope along the thalweg is rather steep (2-3%), similar to many other reservoirs in southern Spain. In September 2009, the Izbor River formed a narrow (ca. 2 m) and shallow channel, discharging ca. 1 m^3s^{-1} into a small 'inflow basin' of 30-40 m wide and 200-250 m long (Fig. 3b). The shoreline at that time, widened suddenly downstream of the inflow basin, to reach nearly 400 m at 600 m distance from the inflow section. The inflowing plume did not enter perpendicular to the shoreline, but forming an angle φ ($\neq 90^o$) which changed from day to day, and even hourly (Figs. 3c,d). Our goal is then to evaluate whether inflow angles could affect or not the initial mixing rates between the river plume and the ambient water, and hence, could determine the fate of inflow water in the simulations.

The model grid was constructed with a bathymetry provided by the local government, using $\Delta x = \Delta y = 2$ m, and $\Delta z = 0.1$ m, with a total number of 86585 wet grid cells. Δt was set to 0.3 seconds, C_d was set to 0.003 (Smith, 2006), and $A_h = K_h \approx 5 \times 10^{-2}$ m^2 s^{-1} (Madsen et al., 1988). The reservoir was initially at rest with horizontal isotherms. A stratified temperature profile collected in-situ on day 253 in 2009 at 20.00 h (not shown) was used to initialize the temperature field in the model. The free surface elevation and temperature gradients were set to zero on the eastern boundary of our computational domain (Fig. 3b). Inflows into the lake were simulated as occurring through a three-layer water column on the western boundary, injecting 19ºC water with a constant flow rate Q_0 = 0.77 m^3s^{-1}. Inflow temperature corresponds to the daily average temperature measured in the field on day 253. Once the hydrodynamic steady state was reached (after ~ 10 h), a conservative tracer − with a concentration C_0 = 100 ppb − was injected with the inflow for 3 hours. A set of 17 simulations were conducted with different inflow angles φ ranging from 0º − when the river entered the basin towards the North (Fig. 3b). − to 180º. The different inflow angles were simulated with the SC-method by prescribing the fractions of the total inflow rate, flowing across the S, E and N faces of the inflow cells. Tracer concentration and velocity fields at a cross-section located 100 m downstream of the inlet (X-1, Fig. 3b) were averaged in time during the last hour of release, and the time-averaged values were used to characterize the level of mixing between the inflowing plume and the ambient water in the inflow basin. Mixing rates between the river and lake water were calculated from average tracer concentrations C in the density current at section X-1, in terms of the mixing ratio $\Gamma = C_0/C$ (Fleenor, 2001). The density current in section X-1 was assumed to represent the layer exhibiting eastward motion.

3. Results and discussion

3.1 Simulations in a straight channel aligned and at an angle with the Cartesian grid

Biases in the free-surface slope were of the same order of magnitude ($\varepsilon_I < 2\%$, Table 2), independently of whether the NF- or the SC-method was used to prescribe boundary conditions. Biases in the simulations conducted in the B-channel were also of the same order of magnitude as in the A-simulations (Table 2). Biases in this case decreased with increasing grid resolution, and they were always $\varepsilon < 5\%$ (Table 2). These sets of simulations suggests that the staircase representation of the lateral boundaries channel affects the solution, but weakly. The SC-method, in general, over-predicted the water surface elevations near the boundaries (Figs. 4a-b). For example, for $C_d = 0.2$, the predicted values of ζ in the reference simulation were 0.25 cm, 0.22 cm and 0.20 cm at a distance of $1\Delta x$, $2\Delta x$ and $3\Delta x$ from the inflow boundary, respectively. The values of ζ at those same distances from the inflow boundary, calculated with the SC-method in the A-channel were 0.93 cm, 0.23 cm and 0.20 (Fig. 4a). Overall, the free surface solution calculated with the SC- and NF- boundary approaches converged within the length of three grid cells both at the inflow and outflow boundaries. The overestimation of ζ at and immediately near to flow boundaries with the SC-method is the result of the source term in the continuity equations (Eqs. 1-2), which generates pressure gradients associated to the slope of the free surface elevation. Outside this boundary region, differences in the free surface solution were ca. 0.1 %.

The streamwise velocity profiles at the center of the channel were logarithmic and differences between surface and bottom velocities increased as C_d increased (Fig. 5). Differences between boundary methods were ε_p < 0.4 % in the A-simulations and ε_p ~ 1% in the B-simulations (Table 3). Errors increased near the inflow and outflow boundaries both in the A- and B- simulations. In sections a and c (Fig 2), for example, the errors in the A-simulations were up to 5 % and 2% respectively. The errors in the B-simulations were similar (8% and 4% in sections a, c) (Table 3 and Figs. 4c-d). Vertical diffusivities K_v and water surface elevations also differed near boundaries. For example, for C_d = 0.2, in section a, the differences in K_v, ε_p, were up to 65% and 90% in the A- and B- simulations, respectively (Fig. 4e). In Section c, though, these differences were only 1% and 7%, for A-and B- simulations, respectively (Fig. 4f).

3.2 Simulations of laterally-unconfined inflows to a lake

In the simulations of laterally-unconfined inflows in Lake Béznar, initial mixing rates downstream of the inflow section Γ varied from 2.9 to 3.4 depending on the inflow angle φ of the river plume (Fig. 6). These estimates of initial mixing rates are in the upper range of possible values reported in the literature. Ryan and Harleman (1971), for example, is one of the earliest references on initial mixing in the plunge region, and report values of Γ ranging from 1.5 to 3.0 in their laboratory experiments. Johnson and Stefan (1988) even report values of Γ as high as 4.5 in their series of inflow laboratory experiments in flat diverging channels, for the largest diverging angles. Despite being higher than previously reported in other lakes − which are, in all cases, below 1.7 (Elder and Wunderlich, 1972; Hebbert et al., 1979; Ford and Johnson, 1983) −, modeled values of Γ agree with field observations in Lake Béznar (Cortés et al., 2014).

In our simulations, initial mixing rates tended to be bigger (Γ > 3.1) for the largest inflow angles (φ > 120º), but smaller (Γ < 3.1) for northward inflows (φ < 120º). The largest dilutions Γ were predicted for φ = 166º, with the river jet pointing south. Dilutions of ca. 2.9 were estimated when the river inflows pointed north (φ < 90º). Those differences of up to 20% in initial mixing ratios can be the result of differences in the extent of the momentum dominated region x_m, near the inflow section, before the river plunges. In this region, river inertia exceeds buoyancy forces and, as a result, large horizontal velocity gradients develop leading to large mixing rates. The distance x_m from the inflow section to the plunge point for a free buoyant jet entering perpendicular to the lake boundaries (i.e. φ ~ 90º) can be estimated from the hydraulic and buoyant characteristics of the inflow, the slope angle of the basin and a lateral entrainment constant, using the semi-analytical model of Hauenstein and Dracos (1984). For Lake Béznar x_m is approximately 100 m, which agrees with the results of our simulations with $\varphi \sim 90^o$ (Fig. 7b). The river forms a free jet for inflows entering nearly perpendicular to the shoreline ($\varphi \sim 90^o$, Fig. 7b). Moreover, in that case, the buoyant jet does not intersect the physical boundary and the momentum dominated region develops freely in the inflow basin. For inflow angles $\varphi \sim 0$ or $\varphi \sim 180^o$ (Fig. 7a and 7c, respectively), in turn, the extent of the momentum dominated region becomes limited by the geometry: the buoyant impinges on the shoreline, as shown by the tracer concentration field at the bottom layer on the inflow basin. Moreover, the jet tends to become attached to the boundaries. Hence, one might expect lower dilution rates for angles $\varphi \sim 0$ or $\varphi \sim 180^o$. Note, though, that the interface at the study section X-1 between the density current and the ambient water tilts at different angles, depending on the inflow angle, as shown by the white line in Figs. 7d, 7e and 7f, based on the longitudinal velocity direction. As a result of differences in the tilt in the interface, one expects differences in the area of contact S_c between the river and lake water and in the shear in the flow field. In general, a larger area of contact between the river and lake water is observed when inflow angles are $\varphi \sim 180^o$ (Fig. 7f). Thus, the magnitude of the vertical eddy diffusivity, and thus the shear between the current and the lake water, at the interface k_{vi} tend to be larger for southward pointing inflows (Figs. 7g and 7h). For example, the average differences between the vertical diffusivity at the interface for two extreme inflow angles (i.e. $\varphi \sim 0$ and $\varphi \sim 180^o$) are 45% higher when the river enters toward the south, and the average differences of the river-lake area of contact are also 30% higher for $\varphi > 120^o$ (Table 4). As a result, maximal mixing ratios are simulated for $\varphi > 120$.

The intrusion depths of the river plumes, and hence, the fate of river-borne substances, as simulated in lake models, might differ depending on the inflow angle used and hence, on the initial mixing rate between lake and river water. Given that river inflows represent one of the major sources of nutrients to river valley reservoirs (Kennedy, 1999), inflow angles might also be important in determining the ecosystem response. In the uncertainty analysis conducted by Ayala et al. (2014) in Lake Béznar with a one-dimensional lake model (Rueda et al. 2007, Chung et al. 2008), the initial mixing ratio was allowed to vary randomly within the range of values reported in the literature, from 1 to 4 (Ayala et al., 2014). The model in that work was used to simulate the fate of river inflows and the loads of river-borne nutrients (phosphorus, in particular) in the surface mixed-layer SML during a period of 180 days in 2010. From those experiments, a set of i = 300 pairs of simulations were selected, with Γ in each pair (Γ_1, Γ_2) differing in 0.5 (i.e. $\Gamma_2(i) = \Gamma_1(i) + 0.5$), as found above for different inflow angles. The intrusion depths were, on average, 10% smaller and the phosphorous loads into the SML were 11% bigger in the simulations conducted with the biggest initial mixing ratios. The maximum differences in P loads could be of up to 100%, at times with peak loading rates. These maximal loads tended to occur, either at the start or the end of the stratification period (Ayala et al., 2014). These differences in P loads were significant in the statistical sense (at the 95% confidence level), and could be important from a water quality modeling perspective, depending on the sensitivity of the phytoplankton growth to nutrient concentration, and depending on the availability of nutrients in the SML. In any case, these results suggest that inflow angles should be accurately represented, at least when dealing with simulations of laterally-unconfined inflows in reservoirs. The SC-boundary method, in these cases, provides a simple and straightforward approach to account for the inflow angel in Cartesian grids.

4. Summary and conclusions

Sources and sinks (SC) in the governing equations defined along flow boundaries can be used in 3D hydrodynamic and transport models to simulate the effects of inflows-outflows. This is an alternative and more flexible approach to define flow-boundary conditions in Cartesian grid models compared to the most commonly used approach (NF) in which velocities that are normal to the boundary faces are prescribed. Using the SC-approach, not only inflow magnitude, but also its direction (whether it is aligned or not with the grid axis) can be correctly represented. The approach was applied to simulate flows along a straight rectangular channel not aligned to the Cartesian axes. The error, when using a second-order space-centered method to discretize momentum advection terms together with the SC-boundary method, is comparable with that existing in the simulations conducted in a channel aligned with the Cartesian axis and using the NF-boundary method. Only near the boundaries, the SC- and the NF- approaches diverge.

In a series of simulations of a small scale negatively buoyant inflow into a reservoir, initial mixing rates between the river and the lake water in the inflow basin appeared sensitive to direction of the inflows. Mixing rates varied up to 20% depending on the inflow angle φ. As a result of the changes in the inflow direction, significant differences in intrusion depth, the timing of entrainment of the intrusions in the surface mixed layer, and consequently, the fate of river-borne substances in the reservoir are likely to occur. Hence, being able to represent inflow inertia and direction in laterally-unconfined inflows is required for accurate predictions of the fate of river-borne substances.

Acknowledgements

The parallel version of the hydrodynamic model was developed under project CGL2008-06101/BOS, funded by the Spanish Ministry of Science and Innovation.

References

Appt, J., Imberger, J., Kobus, H., 2004. Basin-scale motion in stratified Upper Lake Constance. Limnology and Oceanography 49(4), 919–933.

Ayala, A.I., Cortés, A., Fleenor, W.E., Rueda, F.J., 2014. Seasonal scale modeling of the fate of river inflows in stratified reservoir: structural vs. parametric uncertainty in inflow mixing. Journal of Environmental Modelling & Software, 60: 84-98, doi:10.1016/j.envsoft.2014.06.011.

Berger, M. J., Oliger, J., 1984. Adaptive mesh refinement for hyperbolic partial differential equations. Journal of Computational Physics 53(3), 484-512, doi: 10.10016/0021-9991(84)90073-1.

Causon, D. M., Ingram, D. M., Mingham, C. G., Yang, G., Pearson, R.V., 2000. Calculation of shallow water flows using a Cartesian cut cell approach. Advances in Water Resources 23(5), 545-562, doi: 10.1016/S0309-1708(99)00036-6.

Chaudhry, M. H., 1993, Open-Channel flow, Prentice-Hall, Inc, Englewwod Cliffs, New Jersey, 528 pp.

Chung, E. G., Schladow, S. G., Perez-Losada, J., Robertson, D. M., 2008. A linked hydrodynamic and water quality model for the Salton Sea. Hydrobiologia 604, 57-75, doi: 10.1007/s10750-008-9311-6.

Cortés, A., Fleenor, W. E., Wells, M.G., de Vicente, I., Rueda, F.J., 2014. Pathways of river water to the surface layers of stratified reservoirs. Limnology and Oceanography 59(1), 233-250, doi: 10.4319/lo.2014.59.1.0233.

Durran, D. R., 1999. Numerical methods for wave equations in geophysical fluid dynamics, first ed. Springer-Verlag, New York, 465 pp.

Elder, R. A., Wunderlich, W. O., 1972. Inflow density currents in TVA reservoirs. In: Proceedings of the International Symposium on Stratified Flows, Novosibirsk, pp. 221-236.

Fleenor, W. E., 2001. Effects and control of plunging inflows on reservoir hydrodynamics and downstream releases. Ph.D. Dissertation, Univ. of California, Davis, 160 pp.

Ford, D. E., Johnson, M. C., 1983. An assessment of reservoir density currents and inflow processes. Technical Report E-83-7, U.S. Army Corps of Engineers, Waterways Experiment Station, Vicksburg, 110 pp.

Gibou, F., Min, C., Ceniceros, H., 2007. Non-graded adaptive grid approaches to the incompressible Navier-Stokes equations. Fluid Dynamics and Materials Processing 3(1), 37-48.

Ham, F. E., Lien, F. S., Strong, A. B., 2002. A fully conservative second-order finite difference scheme for incompressible flow on nonuniform grids. Journal of Computational Physics 177(1), 117-133, doi: 10.1006/jcph.2002.7006.

Hauenstein, W., Dracos, T., 1984. Investigation of plunging density currents generated by inflows in lakes. Journal of Hydraulic Research 22(3), 157-179, doi: 10.1080/00221688409499404.

Hebbert, B., Patterson, J., Loh, I., Imberger, J., 1979. Collie River underflow into the Wellington reservoir. Journal of Hydraulic Engineering Division105(5), 533-545.

Hodges, B. R., Imberger, J., Saggio, A., Winters, K. B., 2000. Modeling basin-scale internal waves in a stratified lake. Limnology and Oceanography 45(7), 1603-1620, doi: 10.4319/lo.2000.45.7.1603.

Hollan, E., 1998. Large inflow-driven vortices in Lake Constance, in: Imberger, J (Ed.), Physical Processes in Lakes and Oceans, Coastal Estuarine Stud., vol. 54, AGU, Washington, D.C., pp 123–136, doi: 10.1029/CE054p0123.

Hoyer, A. B., Wittmann, M. E., Chandra, S., Schladow, S. G., Rueda, F. J., 2014a. A 3D individual-based aquatic transport model for the assessment of the potential dispersal of planktonic larvae of an invasive bivalve. Journal of Environmental Management 145, 330-340, doi: 10.1016/j.jenvman.2014.05.011.

Hoyer, A. B., Schladow, S. G., Rueda, F. J., 2014b. Local Dispersion of Invasive Bivalve Species by Wind-driven Lake Currents. Submitted to Limnology & Oceanography: Fluids & Environment.

Imboden, D. M., Wüest, A., 1995. Mixing mechanism in lakes, in: Lerman, A., Imboden, D., Gat, J. (eds.), Physics and Chemistry of Lakes. Springer-Verlag, Berlin Heidelberg, pp 83-138.

Johnson, T. R., Stefan, H. G., 1988. Experimental study of density induced plunging into reservoirs and coastal regions. Report 245. St. Anthony Falls Hydraulics Laboratory, University of Minnesota, 178 pp.

Kantha, L. H., Clayson, C. A., 1994. An improved mixed layer model for geophysical applications. Journal of Geophysical Research 99(C12), 25235-25266, doi: 10.1029/94JC02257.

Kennedy, R.H., 1999. Reservoir design and operation: Limnological implications and management opportunities, in: Tundisi, J.G., Straskraba, M. (Eds.), Theoretical reservoir ecology and its applications. Backhuys Publishers, Leiden, pp 1–28.

Laval, B. E., Imberger, J., Findikakis, A.N., 2005. Dynamics of a large tropical lake: Lake Maracaibo. Aquatic Sciences 67(3), 337–349, doi: 10.1007/s00027-005-0778-1.

Liang, Q., Zang, J., Borthwick A. G. L., and Taylor, P. H., 2007. Shallow flow simulation on dynamically adaptive cut cell quadtree grids. International Journal for numerical methods in fluids 53, 1777-1799, doi: 10.1002/fld.1363.

Lynch, D. R., 1986. Basic hydrodynamic equations for lakes, in: Gray, W.G. (Ed), Physics-based modeling of lakes, reservoirs and impoundments, ASCE, New York, pp. 17-53.

Madsen, P.A., Rugbjerg, M.Y., Warren, I.R., 1988. Subgrid modeling in depth integrated flows, in: Proc. 21st Coastal Engineering Conference, ASCE, New York, 1, 505-511.

Mellor, G.L., Yamada, T., 1974. Development of turbulence closure models for planetary boundary layers. Journal of Atmospheric Sciences 31, 1791-1806.

Okely, P., Imberger, J., 2007. Horizontal transport induced by upwelling in a canyon-shaped reservoir. Hydrobiologia 586: 343–355, doi: 10.1007/s10750-007-0706-6

Peng, Y., Mittal, R., Sau, A., Hwang, R., 2010. Nested Cartesian grid method in incompressible viscous fluid flow. Journal of Computational Physics 229(19), 7072-7101, doi: 10.1006/j.jcp.2010.05.041.

Peskin, C.S., 1972. Flow patterns around heart valves: A numerical method. Journal of Computational Physics 10, 252-271.

Peskin, C.S., 2002. The immersed boundary method. Acta Numerica, 11: 479-517, doi: 10.1017/S0962492902000077.

Reckinger, S. M., Vasilyev, O.V., Fox-Kemper, B., 2012. Adaptive volume penalization for ocean modeling. Ocean Dynamics 62(8), 1201-1215, doi: 10.1007/s10236-012-0555-3.

Rueda F.J., Schladow S.G., Pálmarsson, S.Ó., 2003. Basin-scale internal wave dynamics during a winter cooling period in a large lake. Journal of Geophysical Research 108(C3), 3097, doi:10.1029/2001JC000942.

Rueda, F.J., Cowen, E.A., 2005. Residence time of a freshwater embayment connected to a large lake. Limnology and Oceanography 50(5), 1638-1653.

Rueda, F. J., Fleenor, W. E., de Vicente, I., 2007. Pathways of river nutrients towards the euphotic zone in a deep reservoir of small size: uncertainty analysis. Ecological Modelling 202(3-4), 345-361, doi: 10.1016/j.ecolmodel.2006.11.006.

Rueda, F.J., Vidal, J., 2009. Currents in the upper mixed layer and in unstratified water bodies, in:,Likens, G.E. (Ed), Encyclopedia of Inland Waters, vol. 1, Elsevier, Oxford, pp. 568-582.

Rueda, F.J., MacIntyre, S., 2010. Modeling the fate and transport of negatively buoyant storm-river water in small multi-basin lakes, Environmental Modelling & Software 25(1), 146-157, doi: 10.1016/j.envsoft.2009.07.002.

Ryan, P. J., Harleman, D. R., 1971. Prediction of the annual cycle of temperature changes in a stratified lake or reservoir: Mathematical model and user's manual.

Report 137, Parsons, R.M. Laboratory for Water Resources and Hydrodynamics, Massachusetts, 132 pp.

Saiki, E. M., Biringen, S., 1996. Numerical simulation of a cylinder in uniform flow: Application of a virtual boundary method. Journal of Computational Physics 123(2), 450-465, doi: 10.1006/jcph.1996.0036.

Singleton, V.L., Rueda, F.J., Little, J.C., 2010. A coupled bubble plume-reservoir model for hypolimnetic oxygenation. Water Resources Research 46(12), W12538, doi:10.1029/2009WR009012.

Smith, P. E., 2006. A semi-implicit, three-dimensional model of estuarine circulation, Open-File Report 2006-1004, United States Geological Survey, Sacramento, CA, 194 pp.

Vidal, J., Rueda, F. J., Casamitjana, X., 2007. The seasonal evolution of high vertical–mode internal waves in a deep reservoir. Limnology and Oceanography 52, 2656-2667.

Table 1. Functions f(ζ^{n+1}) and g(ζ^{n+1}) for the expression of the volumetric transports U and V at time n+1 in the momentum equations, and source-sink terms E and N, added to f(ζ^{n+1}) and g(ζ^{n+1}) respectively, to prescribe flow in the SC approach.

Term	Discretized form[1,2,3,4]
f(ζ^{n+1})	$U^{n+1}_{i+1/2,j,k} = \hat{U}_{i+1/2,j,k} - g\frac{\Delta t}{\Delta x}\bar{h}^{n}_{i+1/2,j,k}\left(\frac{\bar{\rho}^{n}_{i+1/2,j,1}}{\bar{\rho}^{n+1}_{i+1/2,j,k}}\right)\left(\zeta^{n+1}_{i+1,j} - \zeta^{n+1}_{i,j} + \zeta^{n-1}_{i+1,j} - \zeta^{n-1}_{i,j}\right)$ $+\Delta t\left(A^{n}_{V\,i+1/2,j,k-1/2}\left(\frac{(U/\bar{h})^{n+1}_{i+1/2,j,k-1} - (U/\bar{h})^{n+1}_{i+1/2,j,k}}{\bar{\bar{h}}^{n+1}_{i+1/2,j,k-1/2}} + \frac{(u)^{n-1}_{i+1/2,j,k-1} - (u)^{n-1}_{i+1/2,j,k}}{\bar{\bar{h}}^{n-1}_{i+1/2,j,k-1/2}}\right)\right)$ $-\Delta t\left(A^{n}_{V\,i+1/2,j,k+1/2}\left(\frac{(U/\bar{h})^{n+1}_{i+1/2,j,k} - (U/\bar{h})^{n+1}_{i+1/2,j,k+1}}{\bar{\bar{h}}^{n+1}_{i+1/2,j,k+1/2}} + \frac{(u)^{n-1}_{i+1/2,j,k} - (u)^{n-1}_{i+1/2,j,k+1}}{\bar{\bar{h}}^{n-1}_{i+1/2,j,k+1/2}}\right)\right)$
g(ζ^{n+1})	$V^{n+1}_{i,j+1/2,k} = \hat{V}_{i,j+1/2,k} - g\frac{\Delta t}{\Delta y}\bar{h}^{n}_{i,j+1/2,k}\left(\frac{\bar{\rho}^{n}_{i,j+1/2,1}}{\bar{\rho}^{n+1}_{i,j+1/2,k}}\right)\left(\zeta^{n+1}_{i,j+1} - \zeta^{n+1}_{i,j} + \zeta^{n-1}_{i,j+1} - \zeta^{n-1}_{i,j}\right)$ $+\Delta t\left(A^{n}_{V\,i,j+1/2,k-1/2}\left(\frac{(V/\bar{h})^{n+1}_{i,j+1/2,k-1} - (V/\bar{h})^{n+1}_{i,j+1/2,k}}{\bar{\bar{h}}^{n+1}_{i,j+1/2,k-1/2}} + \frac{(v)^{n-1}_{i,j+1/2,k-1} - (v)^{n-1}_{i,j+1/2,k}}{\bar{\bar{h}}^{n-1}_{i,j+1/2,k-1/2}}\right)\right)$ $-\Delta t\left(A^{n}_{V\,i+1/2,j,k+1/2}\left(\frac{(V/\bar{h})^{n+1}_{i,j+1/2,k} - (V/\bar{h})^{n+1}_{i,j+1/2,k+1}}{\bar{\bar{h}}^{n+1}_{i,j+1/2,k+1/2}} + \frac{(v)^{n-1}_{i,j+1/2,k} - (v)^{n-1}_{i,j+1/2,k+1}}{\bar{\bar{h}}^{n-1}_{i,j+1/2,k+1/2}}\right)\right)$
Source term E	$\Delta t\frac{Q^{n+1}_{FB}}{\Delta y\cdot\sum_{i=i_{BC1}}^{i_{BCend}}\sum_{j=j_{BC1}}^{j_{BCend}}\sum_{k=1}^{km}\left(\bar{h}^{n}_{i,j,k}\right)}\bar{h}^{n}_{i,j,k}\cdot\alpha_E\frac{\delta}{\rho^{n}_{i+1/2,j,k}}$
Source term N	$\Delta t\frac{Q^{n+1}_{FB}}{\Delta x\cdot\sum_{i=i_{BC1}}^{i_{BCend}}\sum_{j=j_{BC1}}^{j_{BCend}}\sum_{k=1}^{km}\left(\bar{h}^{n}_{i,j,k}\right)}\bar{h}^{n}_{i,j,k}\cdot\alpha_N\frac{\delta}{\rho^{n}_{i,j+1/2,k}}$

[1] The overbar on a layer height h or density ρ variable is used to represent a spatial average in the x- or y- direction between adjacent values

[2] The double overbar denotes average of layer heights.

[3] ^ denotes a solution for the layer volumetric transport that includes only the contribution from the advection, Coriolis, baroclinic pressure and horizontal diffusion terms, treated explicitly in the semi-implicit scheme.

[4] α_E and α_N = fractions of total flow across the East and North faces of a water column respectively ($\alpha_E + \alpha_N = 1$).

Table 2. Bias (%) of free surface elevation slopes *I*. A- (channel aligned with the grid) and B- (rotated channel) simulations. The presence of hyphens in the last column indicates that no simulation was performed for the corresponding value of C_d and grid resolution.

Simulations	A		B		
$\Delta x = \Delta y$ (m)	0.1	0.1	0.1	0.05	0.01
BC[1] / C_d	NF	SC	SC	SC	SC
0.002	0.37	1.54	3.6	1.2	1.62
0.004	1.07	0.84	4.1	1.6	-
0.006	1.13	1.15	3.4	2.2	-
0.008	1.33	1.22	3.3	2.2	-
0.02	1.34	1.22	3.3	2.4	0.48
0.04	1.28	1.20	3.3	2.5	-
0.06	1.31	1.23	3.4	2.6	-
0.08	1.33	1.24	3.4	2.7	-
0.1	1.33	1.24	3.5	2.7	-
0.2	1.33	1.25	3.5	2.8	0.91

[1] BC = type of flow boundary approach.

Table 3. ε_p (%) of the streamwise velocity profiles near the inflow section (section a) , at the centre of the channel (section b) and near the outflow section (section c) for solutions with the SC approach. A- and B- simulations. Grid resolution 0.1×0.1×0.12 m.

Section	C_d	A	B
a	0.002	0.11	1.07
	0.02	0.95	1.84
	0.2	5.16	8.32
b	0.002	0.10	1.03
	0.02	0.16	1.19
	0.2	0.25	1.24
c	0.002	0.92	1.03
	0.02	1.91	1.75
	0.2	1.74	3.87

Table 4. Mean modeled values of the area of contact S_c and vertical eddy diffusivities at the interface k_{vi} for different sections ant two different inflow angles φ in Lake Béznar

	k_{vi} (x 10^{-4}) (m^2 s^{-1})		S_c (m^2)	
φ[1] / x_s(m)[2]	14º (N)	166º (S)	14º (N)	166º (S)
20	0.522	0.704	0.7	0.8
30	0.688	1.414	1.0	2.6
40	0.046	3.038	1.6	4.6
50	0.302	3.713	2.2	4.6
60	0.025	1.737	2.8	6.2
70	0.019	6.514	2.8	5.8
80	0.605	7.458	3.2	6.6
90	1.075	5.107	3.0	8.6
100 (X-1)	1.615	5.271	5.0	6.0

[1] N = northward and S = southward;

[2] x_S = Distance from the inflow section.

Fig. 1. (Left) Schematic plot illustrating the entrance of river inflows at an angle with the Cartesian grid and (right) how these river inflows would be specified with the (top right) NF-method and the (bottom right) SC-method. Black arrows show the direction of the real inflows (left) and those prescribed with the NF-method (top right). Squares, circles and triangles show where variables are defined within a given cell. Crossed symbols show the defined variable is set to zero.

Fig. 2. Configuration sketch of the two sets of experiments: set A (top) and set B (bottom), and location of sections a, b and c for the evaluation of velocity profiles.

Fig. 3. (a) Lake Béznar bathymetry with isobaths every 10 m (modified from Vidal et al., 2007). The shadow area marks the inflow basin. (b) Inflow basin with isobaths every meter (computational domain). We define the cross section X-1 and an inflow angle of the plume φ = 90º. (c,d) Photographs of the inflow basin at Lake Béznar during an artificial tracer release experiment undertaken on day 253 in 2009. The inflow angle of the plume φ is marked. These pictures show that the inflow angle φ varied during the dye injection (3 hours).

Fig. 4. (a, b) Free surface elevations (ζ), (c, d) laterally-averaged streamwise velocities (U_S) and (e, f) laterally-averaged vertical diffusivities (K_v) near the inflow (a, c, e) and outflow (b, d, f) boundaries (sections a and c in Fig. 2) for A- and B- simulations and the NF and SC methods to prescribe flow at boundaries. $\Delta x = \Delta y = 0.1$ m, Δz =0.12 m and $C_d = 0.2$.

Fig. 5. Laterally-averaged streamwise velocities (U_S) at the centre of the A- and B- channels ($\Delta x = \Delta y = 0.1$ m and $\Delta z = 0.12$ m) with the NF- and SC- flow boundary approaches; (a) $C_d = 0.002$, (b) $C_d = 0.02$ and (c) $C_d = 0.2$.

Fig. 6. Simulated values of initial mixing rates Γ at X-1 in the inflow basin of Lake Béznar as a function of the inflow angle φ.

Fig. 7. Lake Béznar simulation results averaged during the 3h of tracer injection (t = 10-13 hr). [a,b,c] Tracer concentration field at the bottom layer of the inflow basin; it

describes the pathways of the density current at the inflow basin as a function of the inflow angle, where (a) φ = 14º; (b) φ = 90º; (c) φ = 166º. [d,e,f] Cross sectional X-1 longitudinal velocities (u) field, where the arrows mark the tangential-vertical (v-w) velocity field, considering different inflow angles (d) φ = 14º; (e) φ = 90º; (f) φ = 166º. The white line marks the interface of the density current according to a velocity criterion. [g,h] Cross sectional decimal logarithmic vertical eddy diffusivity ($\log_{10} [K_v]$) field along 6 different cross-sections from the inflow to X-1 (x = 100 m) for two extreme inflow angles (g) φ = 14º (north); and (h) φ = 166º (south). The green arrows correspond to the inflow jet direction.

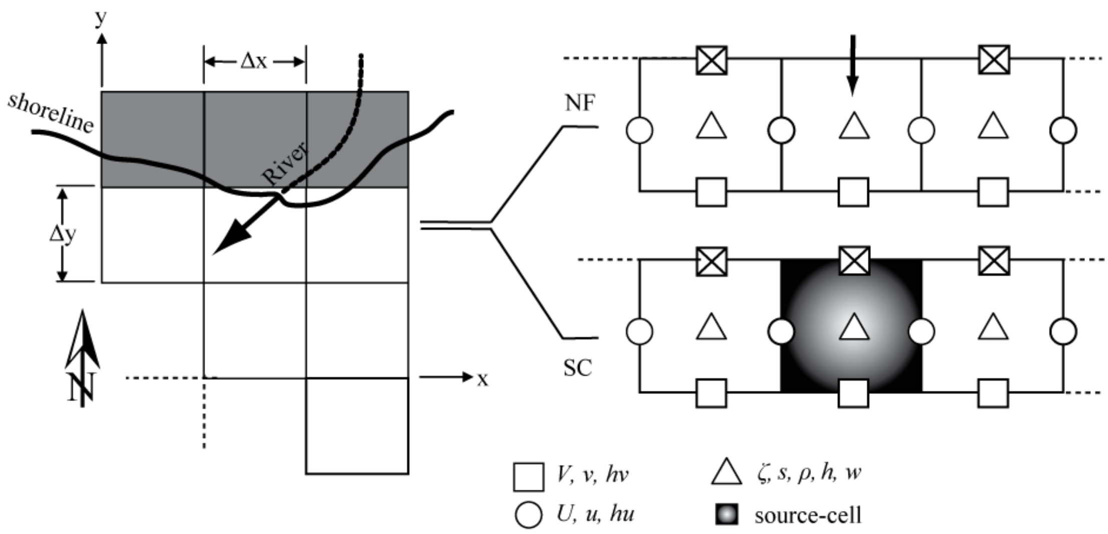

Fig. 1. (Left) Schematic plot illustrating the entrance of river inflows at an angle with the Cartesian grid and (right) how these river inflows would be specified with the (top right) NF-method and the (bottom right) SC-method. Black arrows show the direction of the real inflows (left) and those prescribed with the NF-method (top right). Squares, circles and triangles show where variables are defined within a given cell. Crossed symbols show the defined variable is set to zero.

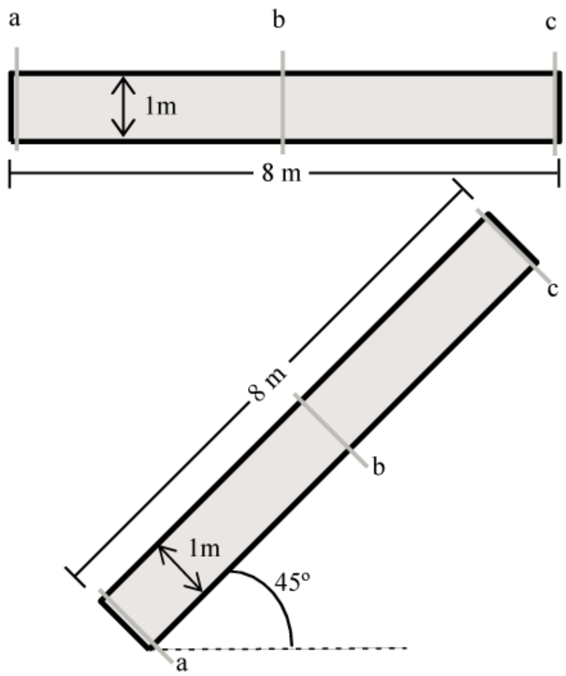

Fig. 2. Configuration sketch of the two sets of experiments: set A (top) and set B (bottom), and location of sections a, b and c for the evaluation of velocity profiles.

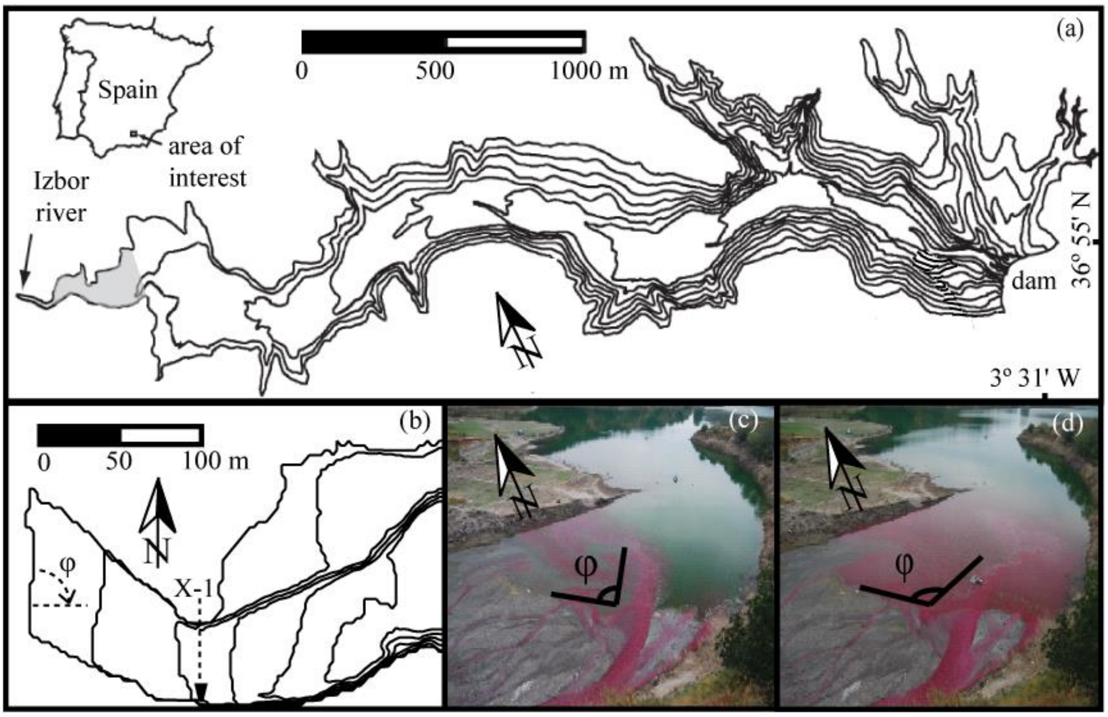

Fig. 3. (a) Lake Béznar bathymetry with isobaths every 10 m (modified from Vidal et al., 2007). The shadow area marks the inflow basin. (b) Inflow basin with isobaths every meter (computational domain). We define the cross section X-1 and an inflow angle of the plume φ = 90º. (c,d) Photographs of the inflow basin at Lake Béznar during an artificial tracer release experiment undertaken on day 253 in 2009. The inflow angle of the plume φ is marked. These pictures show that the inflow angle φ varied during the dye injection (3 hours).

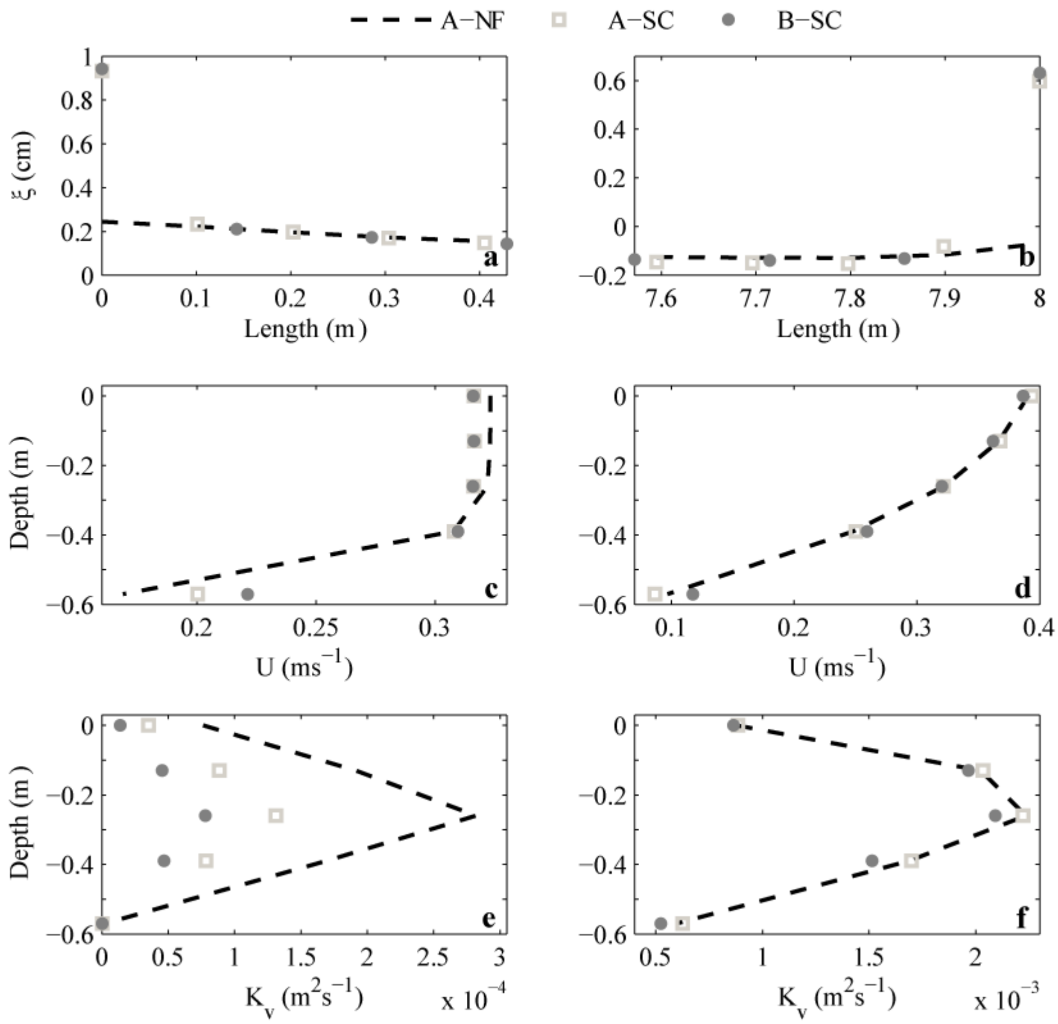

Fig. 4. (a, b) Free surface elevations (ζ), (c, d) laterally-averaged streamwise velocities (U_S) and (e, f) laterally-averaged vertical diffusivities (K_v) near the inflow (a, c, e) and outflow (b, d, f) boundaries (sections a and c in Fig. 2) for A- and B- simulations and the NF and SC methods to prescribe flow at boundaries. $\Delta x = \Delta y = 0.1$ m, $\Delta z = 0.12$ m and $C_d = 0.2$.

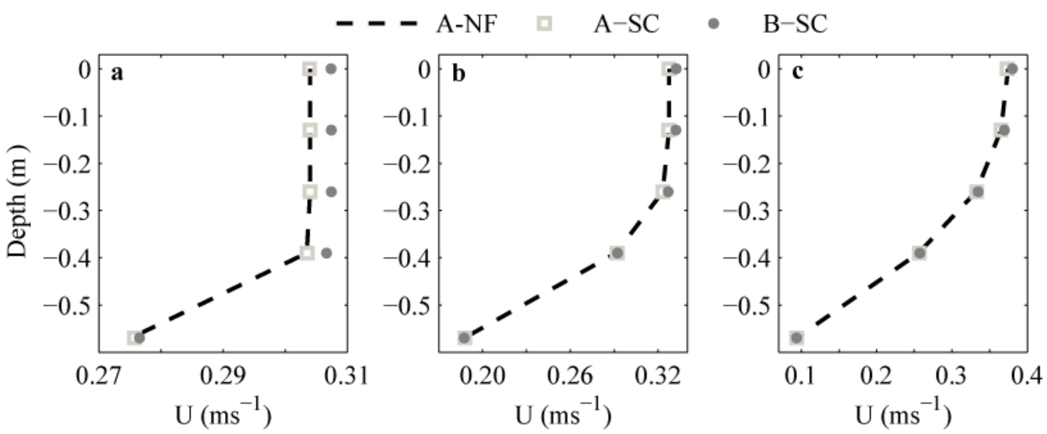

Fig. 5. Laterally-averaged streamwise velocities (U_S) at the centre of the A- and B-channels (Δx = Δy = 0.1 m and Δz = 0.12 m) with the NF- and SC- flow boundary approaches; (a) C_d = 0.002, (b) C_d = 0.02 and (c) C_d = 0.2.

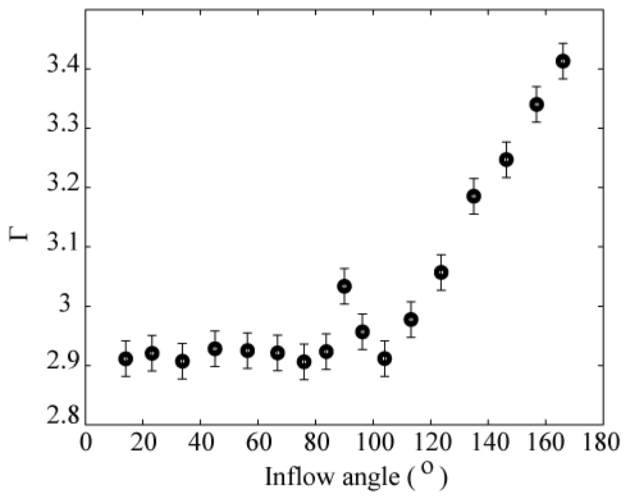

Fig. 6. Simulated values of initial mixing rates Γ at X-1 in the inflow basin of Lake Béznar as a function of the inflow angle φ.

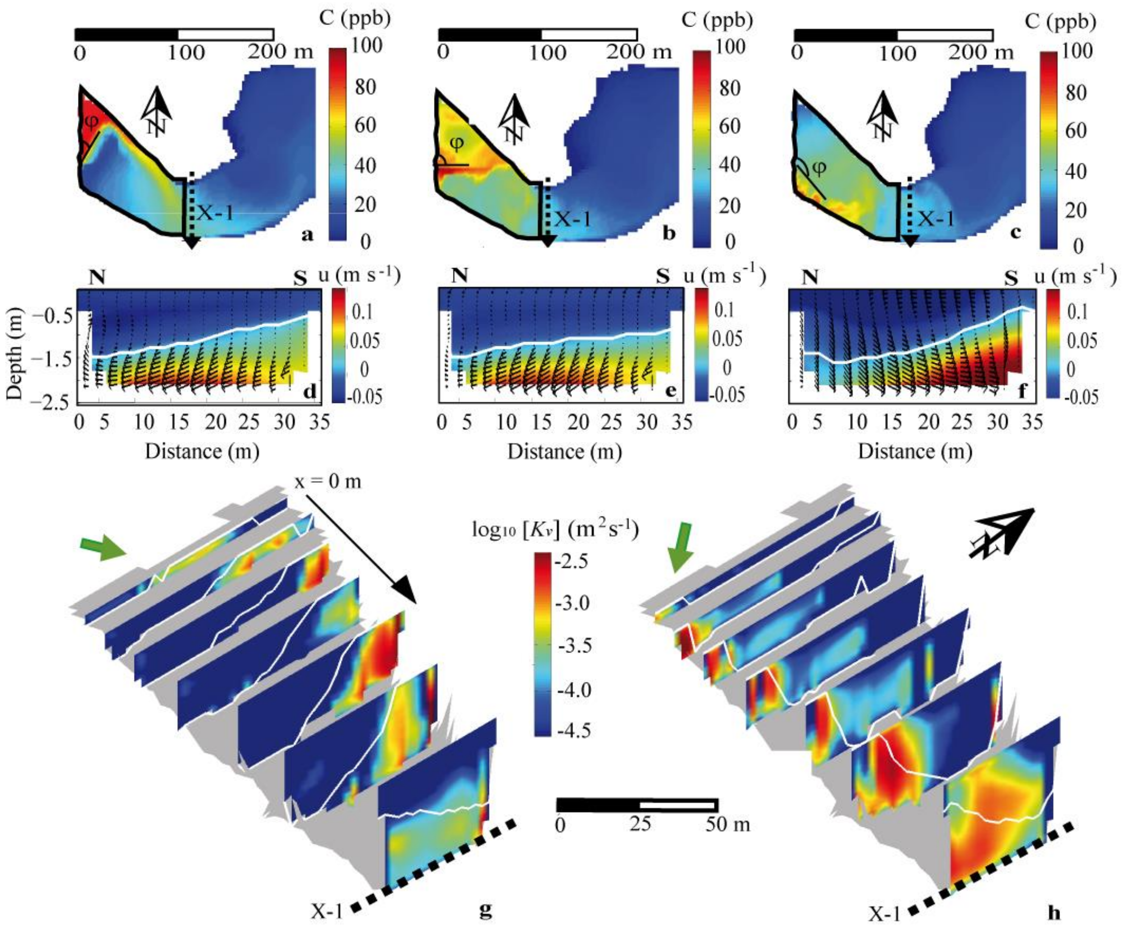

Fig. 7. Lake Béznar simulation results averaged during the 3h of tracer injection (t = 10-13 h). [a,b,c] Tracer concentration field at the bottom layer of the inflow basin; it describes the pathways of the density current at the inflow basin as a function of the inflow angle, where (a) φ = 14º; (b) φ = 90º; (c) φ = 166º. [d,e,f] Cross sectional X-1 longitudinal velocities (u) field, where the arrows mark the tangential-vertical (v-w) velocity field, considering different inflow angles (d) φ = 14º; (e) φ = 90º; (f) φ = 166º. The white line marks the interface of the density current according to a velocity criterion. [g,h] Cross sectional decimal logarithmic vertical eddy diffusivity ($\log_{10}$ [K_v]) field along 6 different cross-sections from the inflow to X-1 (x = 100 m) for two extreme inflow angles (g) φ = 14º (north); and (h) φ = 166º (south). The green arrows correspond to the inflow jet direction.